



JGR Atmospheres

RESEARCH ARTICLE

10.1029/2020JD033284

Key Points:

- Coupled simulations reasonably capture the northward propagation of the BSISO event during July and August 2016
- Sensitivity experiments reveal distinct roles of air-sea interaction and islands in the northward propagation
- Horizontal advection of moisture from reanalysis leads moisture anomalies for the BSISO

Supporting Information:

- Supporting Information S1

Correspondence to:

S. Wang,
sw2526@columbia.edu

Citation:

Wang, S., Sobel, A. H., Lee, C.-Y., Ma, D., Chen, S., Curcic, M., & Pullen, J. (2021). Propagating mechanisms of the 2016 summer BSISO event: Air-sea coupling, vorticity, and moisture. *Journal of Geophysical Research: Atmospheres*, 126, e2020JD033284. <https://doi.org/10.1029/2020JD033284>

Received 12 JUN 2020

Accepted 31 OCT 2020

Accepted article online 20 NOV 2020

Author Contributions:

Conceptualization: Shuguang Wang, Adam H. Sobel
Formal analysis: Shuguang Wang
Funding acquisition: Adam H. Sobel
Investigation: Shuguang Wang
Methodology: Shuguang Wang, Adam H. Sobel
Project administration: Adam H. Sobel
Resources: Shuguang Wang
Software: Shuguang Wang, Shuyi Chen, Milan Curcic
Supervision: Shuguang Wang, Adam H. Sobel
Validation: Shuguang Wang
Visualization: Shuguang Wang
Writing - original draft: Shuguang Wang, Adam H. Sobel, Chia-Ying Lee, Ding Ma, Milan Curcic, Julie Pullen
(continued)

Propagating Mechanisms of the 2016 Summer BSISO Event: Air-Sea Coupling, Vorticity, and Moisture

Shuguang Wang¹ , Adam H. Sobel^{1,2} , Chia-Ying Lee² , Ding Ma¹, Shuyi Chen³, Milan Curcic⁴ , and Julie Pullen⁵

¹Department of Applied Physics and Applied Mathematics, Columbia University, New York, NY, USA, ²Lamont-Doherty Earth Observatory, Columbia University, New York, NY, USA, ³University of Washington, Seattle, WA, USA, ⁴University of Miami, Coral Gables, FL, USA, ⁵Jupiter Intelligence, New York, NY, USA

Abstract During the summer of 2016, a boreal summer intraseasonal oscillation (BSISO) event was observed over Southeast Asia and the South China and Philippine seas. Precipitation anomalies associated with this event propagated northward at a speed of 0.5–1° per day from July to August. To understand the mechanisms, a regional atmosphere-ocean coupled system with the Weather Research and Forecasting (WRF) model and the Hybrid Coordinate Ocean Model (HYCOM) is used to study this BSISO event. The 50-day-long coupled simulations reasonably capture large-scale northward propagation of the event. Coupled simulations with altered air-sea interaction and atmosphere-only simulations with prescribed sea surface temperature illuminate the insignificant role of air-sea interaction within the computation domain in the northward propagation for this event. Diagnostics of the coupled simulation as well as the ECMWF-Interim reanalyses indicate that convection and barotropic vorticity are largely in phase north of 5°N during the event. The BSISO convection is accompanied by moisture anomalies whose magnitudes increase as the BSISO propagates northward. Analysis of the moisture budget shows that positive horizontal advection leads positive moisture anomalies on the intraseasonal time scale north of 10°N. The vorticity-convection relationship, the lead-lag relationship between moisture and its horizontal advection, and the latitude dependence of each for this BSISO event are consistent with general features of BSISO events composited with ECWMF-Interim reanalysis and satellite precipitation data sets.

1. Introduction

The boreal summer intraseasonal oscillation (BSISO) is the dominant mode of intraseasonal variability during the northern summer season in the Tropics (e.g., Krishnamurti & Subramanian, 1982; Lau & Chan, 1986; Yasunari, 1979; B. Wang & Rui, 1990). The BSISO is active primarily over the Indian Ocean, Maritime Continent, and western Pacific. Along its northward and eastward propagation paths, the BSISO brings substantial variations in precipitation, affecting the livelihoods of billions of people in South and Southeast Asia and along the coast of South China (e.g., Chen et al., 2019; Hsu et al., 2016; Li et al., 2015). Accurate prediction of the BSISO is of tremendous socioeconomic value.

Many previous studies have considered the roles of atmospheric and oceanic processes in BSISO propagation, and different propagation mechanisms have been proposed. Broadly, the dominant thinking may be categorized into two groups. One school (e.g., Fu et al., 2003; Kemball-Cook & Wang, 2001; T. Wang et al., 2018; Webster, 1983; Zhang et al., 2018) emphasizes air-sea interaction. Based on the fundamental facts that solar radiation reaching the surface with little loss in clear sky conditions and reduced surface fluxes during BSISO dry phases can produce positive sea surface temperature anomalies on the order of 1°C, these authors have conjectured that the observed warm ocean surface ahead of BSISO convection increases convective instability and initiates nascent convection to its north, thereby forcing the anomalous convection northward. Another school emphasizes the role of large-scale atmospheric dynamical processes and their interaction with convection. Several authors (Bellon & Sobel, 2008a, 2008b; Jiang et al., 2004) have asserted that the BSISO convection tilts the horizontal vorticity associated with the strong vertical shear of monsoonal horizontal flows, generating positive vertical vorticity anomalies north of the BSISO convection and negative ones to its south. These studies all hypothesized that the vorticity anomalies further drive boundary layer convergence and promote convection to the north, although they differ in detail (Bellon & Srinivasan, 2006). In addition, several other studies have suggested that other processes may also

Writing – review & editing:

Shuguang Wang, Adam H. Sobel, Chia-Ying Lee, Ding Ma, Milan Curcic

contribute to northward propagation of the BSISO, including beta drift of zonally localized potential vorticity anomalies generated by convection (Boos & Kuang, 2010) and the momentum flux associated with convection (Kang et al., 2010).

The various mechanisms proposed for BSISO propagation have been assessed to some degree using numerical models. The results from different studies examining the role of air-sea interaction in driving the BSISO are not entirely consistent. Based on an idealized modeling study, Bellon et al. (2008) suggest that an interactive ocean is not crucial. Other studies (Fu et al., 2007; Fu & Wang, 2004) have emphasized the importance of air-sea interaction for dynamics and prediction of the BSISO based on coarse resolution GCM (general circulation model) numerical experiments with parameterized convection. The shear-vorticity-convection mechanism has been shown to work in simplified models (Bellon et al., 2008; Jiang et al., 2004). DeMott et al. (2013) diagnosed all these possible mechanisms in reanalysis and GCM simulations and concluded that each of them might play greater or lesser roles in different regions. Adames et al. (2016) and Jiang et al. (2018) recently assessed the moist entropy budget of the BSISO in reanalysis data and climate models. Those authors found that horizontal advection of moist entropy is the largest contribution to the tendency of moist entropy associated with BSISO and further argue that the BSISO may be treated grossly as a “moisture mode”—similar to its winter counterpart, the Madden Julian Oscillation, despite the differences in their spatiotemporal patterns or propagation directions. This conclusion is provocative in that the study is mute regarding the importance of either the shear-vorticity-convection mechanism or air-sea interaction.

Most of these studies focus on the BSISO in the Indian Ocean. Nevertheless, the BSISO achieves its maximum amplitude in the longitudes of the Maritime Continent and west Pacific Ocean (e.g., Figures 2 and 3; Sobel et al., 2010), where the presence of islands plays important roles in structuring convection. The complex topography, a diverse population of tropical islands, and contrasts between shallow and deep seas in this region are known to drive variability in precipitation across a wide range of temporal and spatial scales (e.g., Pullen et al., 2015). How these lower boundary conditions influence the BSISO convection in the atmosphere and modulate its propagation, however, is largely unknown.

The goal of this study is to clarify some of these mechanisms through a case study. We focus on a BSISO event observed during July and August 2016 in the Maritime Continent region. This event exhibited typical BSISO characteristics in terms of propagation and amplitude (as discussed later from the BSISO indices). This BSISO event also contained two named tropical storms, Nida and Dianamu, within its active phase in the Maritime Continent region. We use an atmospheric ocean-land coupled modeling system to simulate the spatial and temporal evolution of this event in a model with horizontal resolution in the “gray zone,” at which deep convective cloud systems can be partially resolved. Building upon these cloud system-permitting simulations, we further design and conduct sensitivity experiments to assess the roles of the distribution of sea surface temperature, air-sea coupling, and land-sea contrast in the Maritime Continent for the propagation of this BSISO event.

The rest of this article is structured as follows. The data and coupled modeling methodologies are described in section 2. Synoptic analysis of the BSISO event is presented in section 3. Results from the numerical simulations and sensitivity experiments are discussed in section 4. Section 5 discusses the dynamical relationships between vorticity, moisture, and convection. Section 6 contains conclusions and discussion.

2. Data and Methodology

2.1. Regional Coupled Numerical Modeling

We adopt a regional coupled modeling system developed by Chen and Curcic (Chen & Curcic, 2016; Chen et al., 2018a; Curcic et al., 2016; Li et al., 2019) to study the 2016 BSISO event. The coupled system consists of an atmospheric component, the Weather Research and Forecast model V3.8.1 (Skamarock et al., 2008), and an oceanic component, the Hybrid Coordinate Ocean Model V2.2 (HYCOM; Wallcraft et al., 2009). We configure both components to simulate the atmosphere and ocean in the tropical Indian Ocean, Maritime Continent, and Western Pacific Ocean (Figure 1). Both the atmosphere and ocean are constrained to match conditions from global observation-based reanalyses at the lateral boundaries through relaxation. Five grid points are used in the transition zone for the relaxation, and the relaxation is applied to winds, temperature, and humidity for WRF. Similar relaxation is done to HYCOM but for currents, temperature, and salinity.

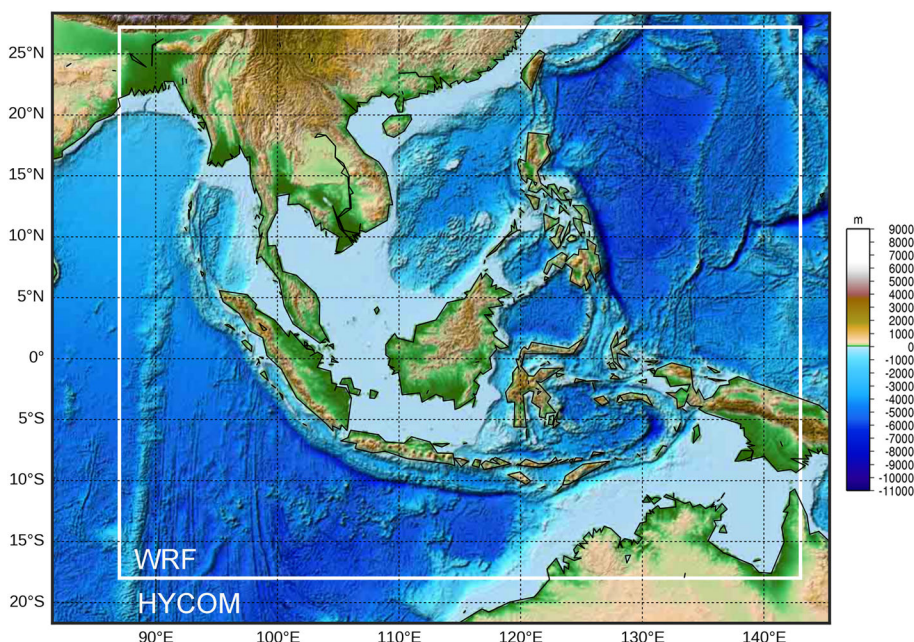


Figure 1. Computational domains used for HYCOM and WRF. Shading indicates the topography and bathymetry (m).

The advantage of this regional modeling approach, compared to a global modeling approach, is that errors outside of the region of interest (as found in the global models) are kept relatively small throughout the numerical integrations such that errors outside domain have minimal influence on the quality of the numerical simulations. Focusing on a specific region also allows better computational efficiency, allowing higher resolution for a given computational cost.

WRF and HYCOM exchange momentum and heat at the interface between the atmosphere and ocean. HYCOM also takes freshwater input from WRF-produced precipitation. Sea surface temperature is a dynamically evolving variable in the simulations. The coupling method and its performance for tropical cyclones are documented by Chen and Curcic (2016) and Curcic et al. (2016). The ERA-Interim reanalysis (Dee et al., 2011) is used to construct the initial conditions and lateral boundary conditions for WRF. The global HYCOM reanalysis data, HYCOM + NCODA Global 1/12° Reanalysis, version GLBa0.08 91.2 is used to construct the initial conditions and lateral boundary conditions for HYCOM.

The computational domain of HYCOM covers the Maritime Continent, from 20°S to 27°N and 85°E to 150°E, as shown in Figure 1. Its horizontal grid spacing is 0.08°. A total of 41 hybrid sigma vertical levels are used with 10 levels in the top 50 m. The total number of grid points is $800 \times 650 \times 41$ in longitude, latitude, and depth, respectively. In an earlier phase of this study, we also tested a configuration with 32 vertical sigma levels with five levels in the top 50 m, the same configuration used by the HYCOM consortium to produce the global HYCOM GLBa0.08 reanalysis version 91.2. These tests with 32 vertical levels will be also briefly discussed.

The WRF model is configured to use the following physical parameterization schemes. Surface and soil temperature over land are parameterized using the Unified NOAH land surface physics scheme (Chen & Dudhia, 2001). Shortwave radiative fluxes are parameterized using the RRTMG (Rapid Radiative Transfer Model for GCMs) shortwave radiation scheme (Iacono et al., 2008), and the RRTMG scheme is used for long-wave radiative fluxes. Subgrid-scale vertical turbulent eddy mixing is parameterized using the Asymmetric Convective Model, version scheme (Pleim, 2007). The WRF-Double-Moment double moment scheme is used for cloud microphysics (Lim & Hong, 2010). Surface fluxes are treated using the Monin-Obukhov scheme.

The computational domain of WRF is slightly smaller than that of HYCOM. In the vertical, the WRF domain is discretized into 45 vertical levels, with nine levels in the lowest 1 km and a nominal top at 20 hPa. The

Table 1
Summary of Numerical Experiments and Corresponding Figures

Experiments	Description
ensemble coupled runs	Initialized at July 9, 10 (C10), 11, 12; Figures 5 d, f, 6b,
Uncoupled run	SST from ERAI, July 10, Figure 7(b)
Uncoupled run	SST from C10, Figure 7(c)
Uncoupled run	time mean SST from C10, Figure 7(d)
Coupled run	topography set to 0 over the MC region, Figure 8(b)
Uncoupled run	topography set to 0 over the MC, SST from C10, Figure 8(c)
Uncoupled run	no MC, SST from C10, Figure 8(d)

Note. The initialization date is 10 July 2016 unless stated otherwise. The coupled simulations refer to the WRF and HYCOM coupled experiments. The uncoupled runs refer to the WRF experiments with prescribed SST.

horizontal grid spacing is 9 km, in the so-called “gray zone.” This allows the model to partly resolve organized cloud systems and mesoscale circulations, as well as their upscale impact and coupling with large-scale dynamics. No convective parameterization scheme is used, following prior studies that used the same horizontal resolution with no convection scheme to simulate the MJO (Chen et al., 2018b; Miura et al., 2007; Nakano et al., 2015; S. Wang et al., 2015; Zhang et al., 2017). The total number of grid points in the atmosphere is $600 \times 500 \times 45$ using a type C computational mesh.

A four-member ensemble of coupled simulations was conducted, with start dates varying from 9 to 12 July. Each simulation was integrated until 31 August. Sensitivity experiments were performed based on the coupled run starting from 10 July, and this base run will be referred to as C10. A number of atmosphere-only simulations were also conducted to assess the role of air-sea coupling, by suppressing it and comparing the results with those of the coupled simulations. The lower boundary conditions for these atmosphere-only simulations were taken either from the 6-hourly SST (sea surface temperature) from ERA-Interim (Dee et al., 2011; Donlon et al., 2012) or the 6-hourly SST from one of the coupled simulations. Table 1 summarizes the coupled and uncoupled experiments.

2.2. Observational Data

The ECMWF-Interim (Dee et al., 2011) reanalysis data were used to analyze the synoptic conditions in the atmosphere. A 15- to 90-day Lanczos bandpass filter was used to extract intraseasonal signals. As measures of convection, we also use surface precipitation from the Tropical Rainfall Measuring Mission (TRMM) 3B42 product version 7A (Huffman et al., 2007) and outgoing longwave radiation (OLR) from the NOAA interpolated daily 2.5 resolution OLR data set (Liebmann & Smith, 1996). The HYCOM 1/12° global analysis was used for the ocean, as will be discussed below.

3. Overview of the July and August 2016 BSISO

Figure 2 shows the 15- to 90-day bandpass-filtered OLR and horizontal winds at 850 hPa every 5 days from 5 July to 28 August 2016. The area south of the equator is convectively suppressed during the first 10 days of July. By the middle of July, convective anomalies extending from central eastern India to northwest Australia have become established, signaling BSISO convective initiation, while dry conditions are prevalent in the South China Sea region north of the convective anomaly. The northwest-southeast tilted pattern of both active and suppressed anomalies is typical of the BSISO, as has been identified from EOF analysis (e.g., Kiladis et al., 2014; Kikuchi et al., 2012, Lee et al., 2013; S. Wang et al., 2018), but it is not present all the time. Over the next 30 days, the convective anomaly propagates northward and exhibits considerable variation in its spatial shape. By 25 July, the convective anomaly is found along the equator but then becomes weak and oriented zonally. After crossing the equator, the convective anomaly and its low-level cyclonic circulation gradually strengthen, reaching their peak amplitudes in mid-August. After that time, the active phase dissipates quickly, and by the end of August, the SCS region is dominated by dry conditions.

The complex pattern of the BSISO event may be simplified using daily indices derived from empirical orthogonal functional (EOF) analysis of the relevant variables. Figure 3 shows phase diagrams derived from three BSISO indices that of Kikuchi et al. (2012), which is based on OLR; the OLR-based MJO index (OMI) by Kiladis et al. (2014); and the BSISO1 index by Lee et al. (2013). The OMI index is included here as our prior work (S. Wang et al., 2018; S. Wang et al., 2019) has shown that it represents northward propagation well during the northern summer season. The BSISO-K12 and OMI-K14 both show that this BSISO index begins with amplitude greater than 1 in phases 4 or 5 in early July and rotates anticlockwise in July and August. The BSISO1 index is noisy and rotates clockwise—erroneously—in July. This opposite sense of propagation, compared to the other indices as well as to our expectation of typical BSISO events, is consistent with a lack of propagation exhibited more broadly by this index as shown using correlation analysis by S. Wang et al. (2018).

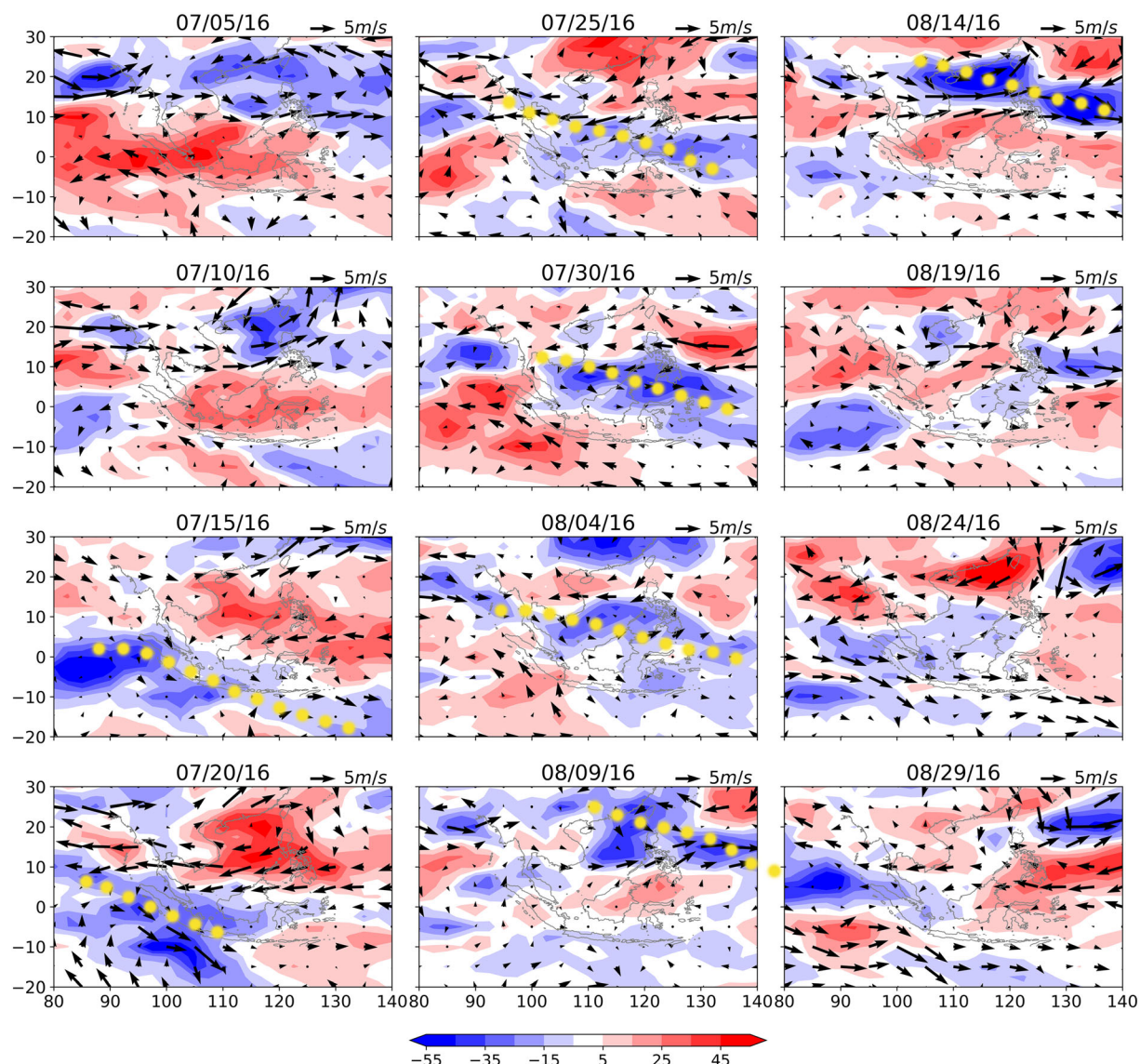


Figure 2. Intraseasonal OLR anomalies (W/m^2 , shaded) and wind vectors at 850 hPa from July to August 2016. A 15- to 100-day bandpass filter is applied to calculate intraseasonal OLR and horizontal winds. The yellow dots indicate the northwest-southeast tilted rain bands.

The precipitation anomaly during this BSISO event shows coherent northward propagation, consistent with the OLR anomaly reconstructed from OMI (Figure 4). The time-latitude diagram of 3-hourly precipitation averaged between 110°E and 130°E shows that the surface rain rate occasionally reaches 20 mm/day during the active phase's northward propagation. The magnitude of the bandpass-filtered precipitation anomaly is ~ 4 mm/day, providing a measure of the amplitude of this BSISO event. The rapidly northward propagating synoptic feature during last few days of July is associated with Tropical Storm Nida. Nida formed on 28 July to the east-southeast of Manila, Philippines, when the BSISO convective phase was located at those latitudes. Nida then moved north-northwestward and made landfall over the Dapeng Peninsula of Shenzhen, China, as a severe tropical storm on 2 August ([https://en.wikipedia.org/wiki/Tropical_Storm_Nida_\(2016\)](https://en.wikipedia.org/wiki/Tropical_Storm_Nida_(2016))). The enhanced rain rates during mid-August (Days 35–40, from a start date of 10 July), around 20°N , are partly associated with another tropical storm, Dianamu, which was also linked to this BSISO event. The system that would become Dianamu was noted by the United States Joint Typhoon Warning Center (JTWC) first on 14 August,

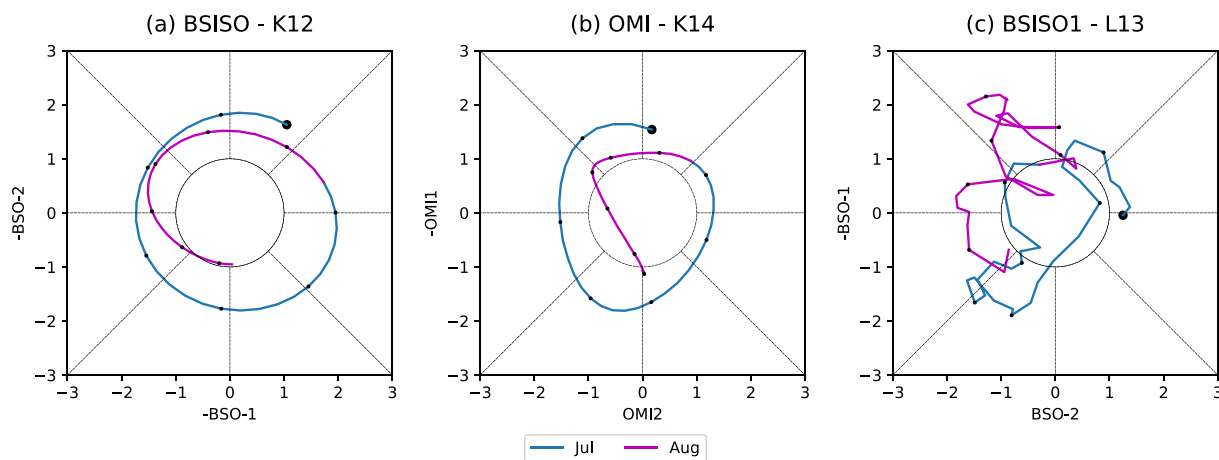


Figure 3. BSISO indices: K12 (a; Kikuchi et al., 2012), OMI (b; Kiladis et al., 2014), and BSISO1 (c) by Lee et al. (2013). Blue: index in July 2016; Magenta: index in August 2016. The blue dots denote the starting point.

when it was located 175-km south of Hong Kong, China, by when the BSISO convective phase had reached its northernmost latitudes. Dianamu moved westward, was named on 18 August, and made landfall on 18 August in northern Vietnam.

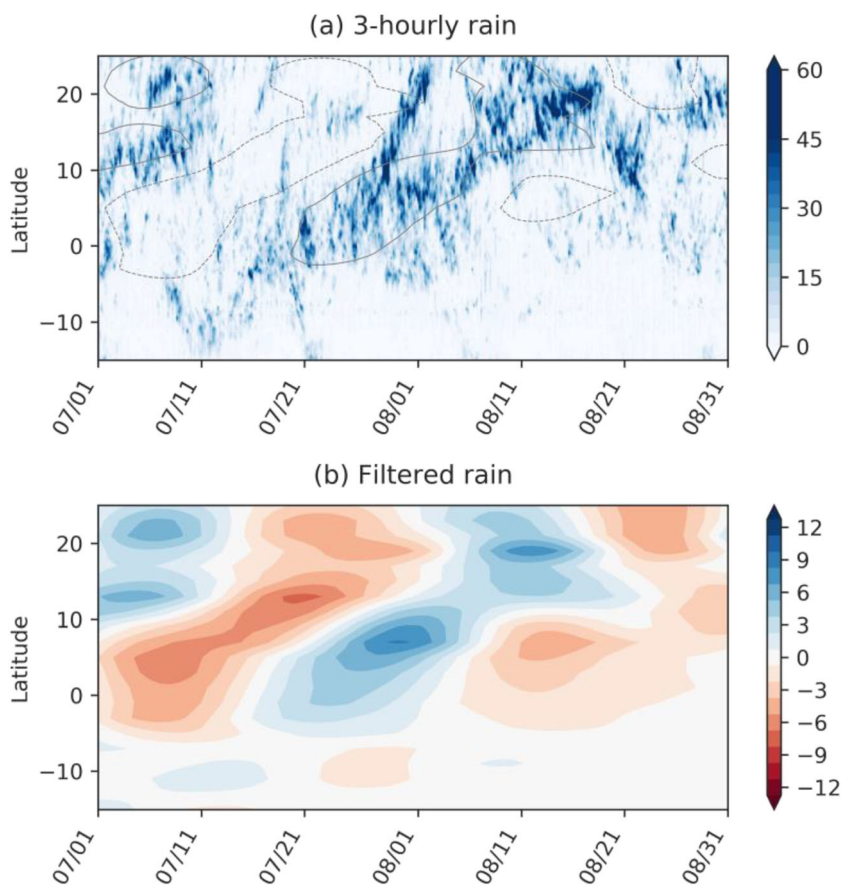


Figure 4. (a) TRMM 3B42 precipitation (3-hourly, 0.25° ; mm/day) between 110°E and 130°E . (b) The 20- to 70-day bandpass-filtered rain anomaly on the same domain as in (a). The gray contours in (a) indicates filtered rain anomalies at -3 and 3 mm/day.

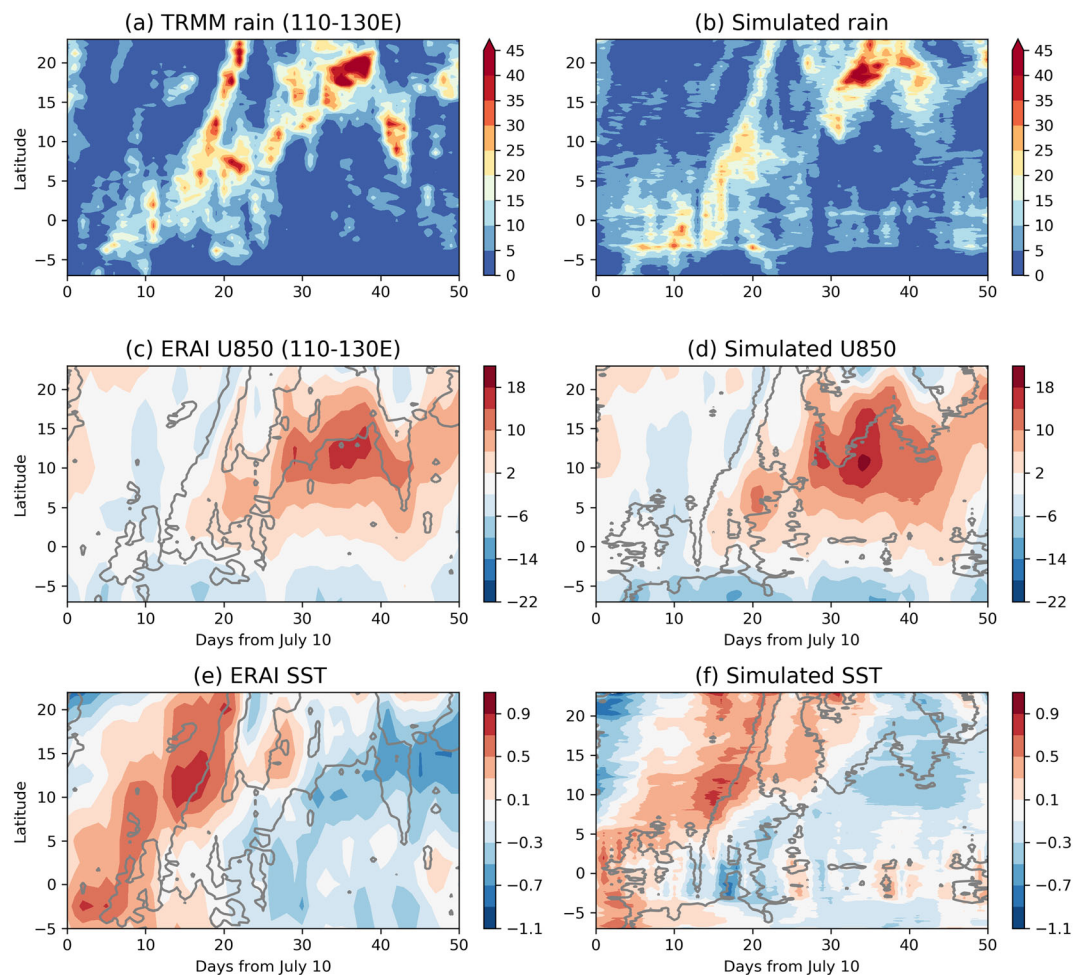


Figure 5. Left: (a) TRMM precipitation, (c) U850, and (e) anomalous surface skin temperature averaged over 110–130°E from ERA-I. Right panels: as in left panels but for ensemble averaged values from the coupled runs. Gray solid contour in the right panels denotes precipitation (10 mm/day).

4. Coupled Simulations

4.1. Propagation of BSISO in the Coupled Simulations

TRMM precipitation and ensemble mean precipitation from the coupled simulations, both averaged over 110–130°E, are shown in Figures 5a and 5b. The model reasonably captures the observed northward propagation from 10 July to the end of July (first 20 days) and after 10 August (Day 30). The propagation is more disrupted between Days 20 and 30, after the tropical storm, in the model compared with the observations.

Time-latitude patterns of U850 are consistent between simulations and ERA-I: Monsoon easterlies are present south of the equator while relatively weak easterlies (<10 m/s) are found between 0°N and 20°N in the first 20 days, and then strong westerlies (~20 m/s) are found from 10°N to 20°N in August. The transition from easterlies to westerlies indicates northward propagation, occurring similarly in simulations and reanalysis. The magnitude of the westerlies is greater than that of the easterlies, presumably because of the background monsoon westerlies in the lower troposphere superimposed on northward propagating anomalies.

Figures 5e and 5f show the propagating surface temperature anomalies in the SCS region (averaged between 110°E and 130°E), computed by subtracting the time mean during this period from the ERAI and coupled ensemble runs. Because land occupies only a small fraction of the total area, this field can be considered roughly equivalent to the sea surface temperature. Anomalies from ERAI reach 1 K at 10°N around Day 15 (near 25 July) when the BSISO rain anomaly is centered near 5°N. Simulated surface temperature

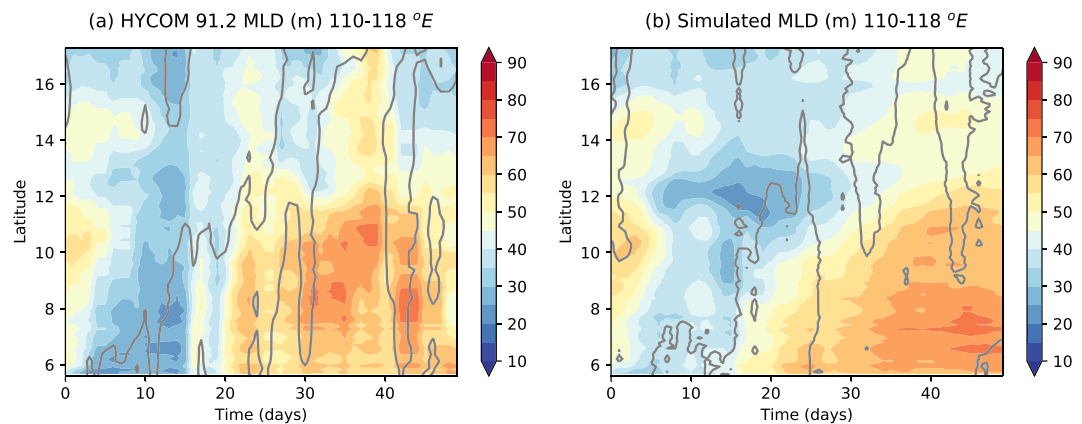


Figure 6. (a) Mixed layer depth (meters, shaded) and precipitation (contour, 7.5 mm/day) averaged between 110°E and 118°E in South China Sea ($5.5\text{--}17.5^{\circ}\text{N}$) from the HYCOM GLBa0.08 global analysis. (b) As in (a) but from the coupled simulations.

anomalies show a similar propagating pattern, but the amplitudes of the positive surface temperature anomalies at 10°N are significantly weaker (0.6 K) than those in observations and so are the negative temperature anomalies that occur after the peak of the BSISO rain episodes. We perform a quantitative comparison between the numerical simulations and the observations using pattern correlation in latitude and time, as shown in Figure 5, after linearly interpolating these variables onto a common grid (every 2°). The pattern correlation reaches 0.95 for U850 (Figures 5c and 5d) between ERAI and the ensemble mean, 0.73 for the SST anomalies (Figures 5e and 5f), and 0.65 for daily precipitation (Figures 5a and 5b) comparing TRMM precipitation to the ensemble mean from the simulations. Based on these pattern correlation coefficients and visual inspection, we conclude that the coupled simulations capture the pattern of northward propagation reasonably well.

Sea surface temperature is closely related to the properties of the ocean mixed layer. Figure 6 shows the mixed layer depth (MLD), diagnosed from a potential density jump exceeding 0.05 kg/m^3 down the water column, from the HYCOM global analysis and the coupled simulations. The MLD from the HYCOM global analysis (Figure 6a) is $\sim 20\text{--}30 \text{ m}$ in the southern SCS region (averaged between 110°E and 118°E) prior to the peak BSISO precipitation and increases to $\sim 70 \text{ m}$ afterward, due to turbulent mixing induced by winds and heavy precipitation. The amplitude of the MLD variations in the SCS is notably smaller north of 12°N . The gradual deepening of the MLD is typical during northward propagation of intraseasonal oscillations in the Indian Ocean basins (e.g., Li et al., 2017) and is presumably a response to atmospheric forcing. Figure 6b shows the same quantity from the coupled simulations. Compared to the analysis, the coupled simulations show a similar deepening of the MLD, but the simulated MLD is overall shallower than that in the analysis by $\sim 5\text{--}10 \text{ m}$ after the passage of BSISO. This implies a smaller bulk heat capacity of the mixed layer in the simulations. It is difficult to identify the source of this discrepancy, given that the MLD from HYCOM analysis is a primarily a modeling product with relatively coarse resolution, and the lack of in situ observations.

4.2. Experiments With Specified SST

As discussed in section 1, the warm SST anomalies leading the BSISO convection may be important drivers of BSISO propagation, and it is possible that the weaker SST anomalies in the coupled simulations without convective parameterization are the cause of the model bias in the modeled precipitation anomalies. We test this hypothesis with atmosphere-only numerical experiments with specified SST. We perform experiments using SST from both reanalysis and C10, a coupled run that was initialized on 10 July. Figure 7a shows U850 and precipitation from the coupled run on 10 July. An atmosphere-only run with ERAI 6-hourly SST (Figure 7b) simulates similar northward propagation in U850 and precipitation but with stronger westerly winds at lower levels, larger precipitation anomalies, and slightly faster propagation speed, particularly at day 30. An atmosphere-only experiment with 6-hourly SST from the coupled run produces very similar rain and U850 compared to the 10 July coupled run (Figure 7c). One way to test the influence of the intra-seasonal variation in the SST on northward propagation is to completely remove that variation in

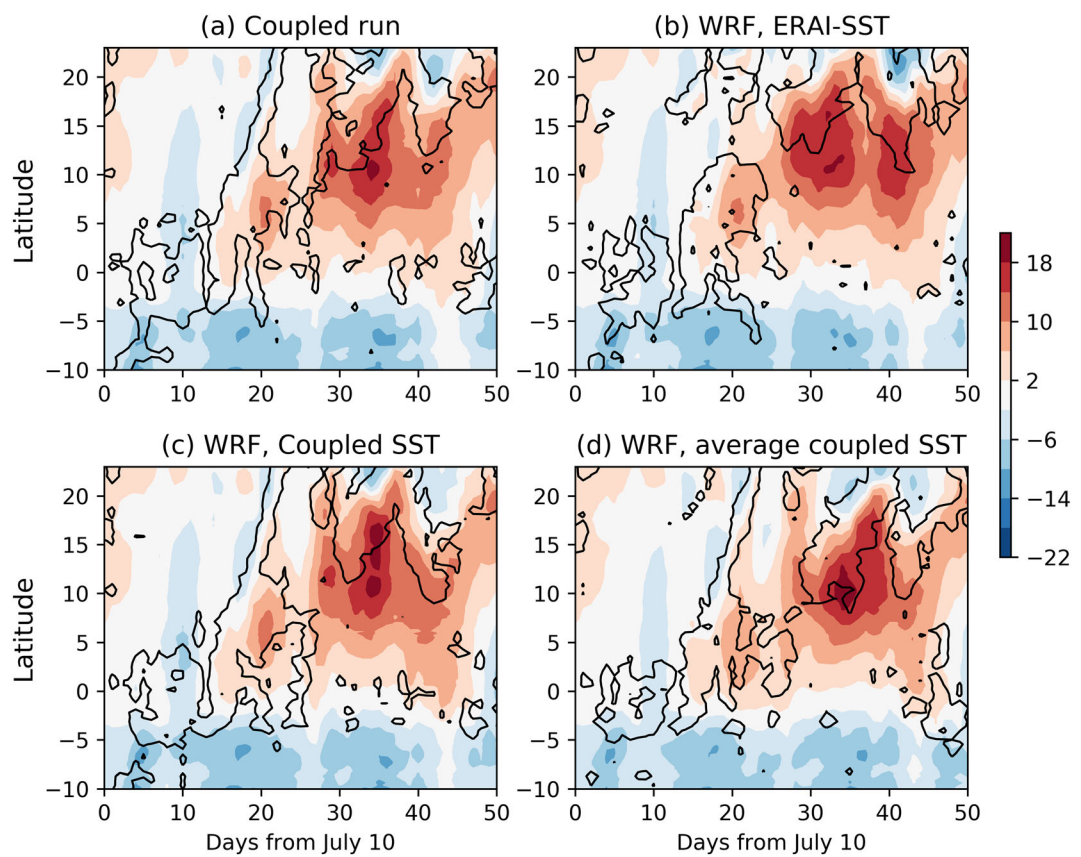


Figure 7. Time-latitude diagram of precipitation (contoured at 10 mm/day) and U850 (shaded, m/s) averaged between 110°E and 130°E from (a) the coupled run initialized on 10 July. (b) Uncoupled run with ERAI SST. (c) Uncoupled run with CSST (coupled SST). (d) Uncoupled run with time mean CSST. Precipitation is averaged every 45 km in the meridional direction and smoothed with a 5-day running average.

atmosphere-only simulations. Figure 7d shows results from one such run, using time-averaged SST taken from the coupled run. This figure shows a propagation pattern similar to that in observations in the low-level wind and precipitation but with somewhat slower northward propagation notable after Day 30, north of 15°N. These simulations without ocean coupling demonstrate that intraseasonal variations in SST play only a small role in determining the propagation speed and amplitude of this BSISO event.

The sensitivity to intraseasonal SST may be misrepresented if the number of vertical levels used in the ocean model is inadequate. We initially performed both coupled simulations and sensitivity experiments using 32 vertical levels in HYCOM, with only five levels in the top 50 m. These sigma levels are the same as those used by the HYCOM consortium to produce the global HYCOM GLBa0.08 reanalysis version 91.2. Northward propagation in the coupled simulations (control) is not much altered by the reduced number of vertical levels (supporting information). However, the corresponding experiment without intraseasonal variations in SST (i.e., using the time-averaged SST field from the corresponding coupled run) shows a significant disruption of the northward propagation in the precipitation field. The large difference between the SST sensitivity experiments at the two different vertical resolutions may be attributed to a larger cold bias in the SST when fewer vertical levels are used (Figure S2 in the supporting information). The greater sensitivity from the 32-level experiments would have led to the misleading conclusion that intraseasonal SST plays an important role in this BSISO event, contrary to the inference drawn from the improved 41-level experiments. Whether the conclusion that ocean coupling is unimportant applies only to the current case or is generally true of other BSISO events remains unclear. Our experiments do suggest, however, that caution should be used interpreting results from coupled numerical experiments with inadequate vertical resolution.

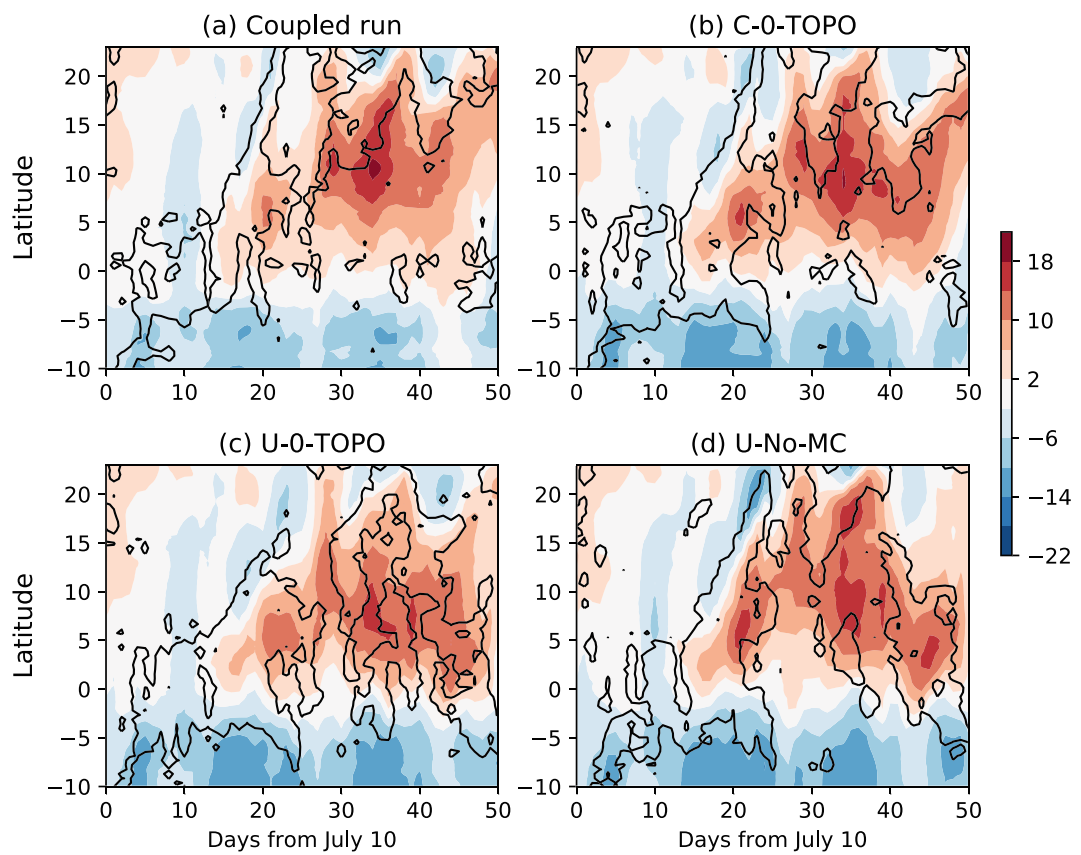


Figure 8. Time-latitude diagram of precipitation (10 mm/day) and U850 (shaded, m/s) averaged between 110°E and 130°E from (a) the coupled run initialized on 10 July. (b) Coupled run with zero topography. (c) Uncoupled run with zero topography. (d) Uncoupled run without islands. Precipitation is averaged every 45 km in the meridional direction and smoothed with a 5-day running average.

4.3. Experiments With Altered Topography

The MC (Maritime Continent) region is home to many islands, some with complex topography, and the highest elevations on some of the islands (e.g., Sumatra) exceed 3,000 m. While these islands differ greatly from one another in both horizontal area and elevation, even relatively small ones drive significant diurnal variability that shapes the precipitation climatology (e.g., Sobel et al., 2011; S. Wang & Sobel, 2017). We examine the effects of topography and the presence of islands on the BSISO with two types of numerical experiments. In one set of experiments, we removed the topography in the MC region (including the Indonesian and Philippine archipelagos) but kept the surface properties the same (surface albedo, land types etc.). Linear interpolation/extrapolation was used to create the initial conditions for the wind field near the surface where the topography was removed. These experiments were performed for both coupled and atmosphere-only configurations, and we refer to them as zero-topography experiments. In a second set of experiments, we completely removed the islands in the MC region. Experiments of this type were conducted solely in the atmosphere-only configuration. Sea surface temperatures in the regions where the islands were removed were produced by interpolation from SST generated in a coupled run. These no-island experiments, while possible in the coupled model, were not conducted in that configuration due to technical difficulties in creating appropriate oceanic initial conditions over the region.

Figure 8b shows the coupled simulation with zero topography in the Maritime Continent region, initialized on 10 July. Compared to the otherwise identical coupled run with topography (Figure 8a), the low-level zonal wind averaged between 110°E and 130°E is considerably stronger: The easterly winds south of the equator reach -10 m/s, and the westerly areas (e.g., over which the westerly winds exceed 10 m/s) expand. The enhanced low-level wind speed is expected due to reduced frictional drag in the absence of topography.

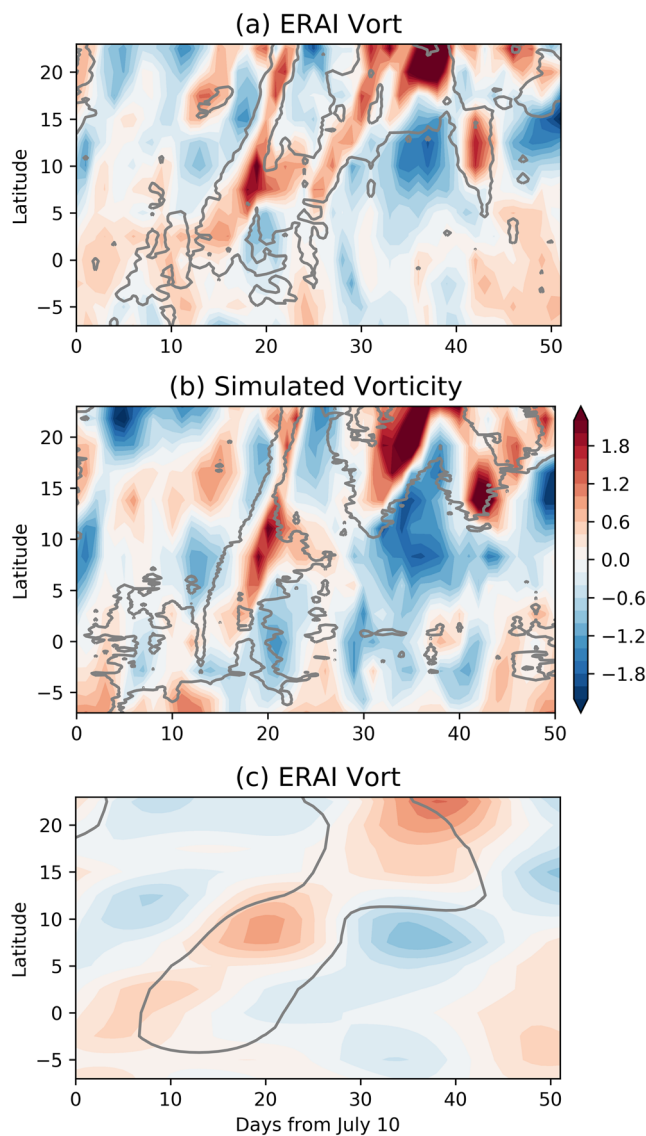


Figure 9. (a) Relative vorticity (10^{-5} s^{-1} , shaded) from ERAI and rain (contour, 10 mm/day) from TRMM, both averaged between 800 and 200 hPa, 110–130°E. (b) As in (a) but from the ensemble mean of the coupled run. (c) As in (a) but for 20- to 90-day bandpass-filtered fields. The gray contour in (c) indicates 2 mm/day.

main feature—a lack of any appreciable delay between vorticity and precipitation on the intraseasonal time scales—remains the same. While the two fields are largely in phase, there are some positive vorticity anomalies during the first 20 days around 10–20°N and negative vorticity anomalies immediately to the south. Given the overall in-phase relationship, however, it is difficult to attribute the northward propagation of this BSISO event to the phase relationship between vorticity and convection described in earlier studies. While we have so far shown only a single BSISO event, we will address its representativeness below using the long-term ECMWF reanalysis and TRMM precipitation data sets.

5.2. Moisture

Northward propagating moisture anomalies associated with the 2016 BSISO event are seen in both the ERA-I reanalysis and the coupled numerical simulations. Figure 10 shows moisture anomalies from ERAI and the coupled ensemble averaged over 110–130°E. Northward propagating moisture anomalies are coherent with propagating precipitation anomalies in both, although somewhat less continuous in the model.

On the other hand, comparison of the contours of the 10 mm/day in rain between the two simulations indicates that the northward propagation does not change appreciably when topography is removed. This run illustrates that topographic drag reduces the magnitude of the zonal winds but has little effect on precipitation.

A zero-topography experiment with prescribed 6-hourly SST taken from a coupled run (Figure 8c) simulates rain and U850 at 110–130°E propagating northward continuously from 10°S to 20°N, but the amplitude of its northward propagating component decreases between 15°N and 20°N, unlike in the coupled runs (Figure 8b). We further remove the islands in the MC region to test the effect of land, as described above. Figure 8d shows that rain arrives at the 15–20°N latitude band around Day 30 in this simulation, compared to Day 40 in both the coupled and uncoupled runs with islands (Figure 8c), indicating a slightly faster northward propagation speed without islands. Both of these runs also show some southward propagating anomalies after the northward propagating anomalies reach 15–20°N. Overall, these sensitivity experiments suggest that the islands in the MC region function primarily as momentum sinks. These results may be viewed in contrast to those from the experiment without intraseasonal variations in SST (Figure 7d); the changes in the experiments with modified topography are larger, suggesting that air-sea coupling is less important than are land processes in the MC region.

5. Convection, Vorticity, and Moisture

5.1. Phase Relationship Between Convection and Vorticity

A number of authors (Bellon & Sobel, 2008a; Jiang et al., 2004; B. Wang & Xie, 1997) have hypothesized that barotropic vorticity, generated from the interaction of convection with the strong monsoon vertical shear of the horizontal winds, leads to boundary layer convergence north of the convection through Ekman pumping. The boundary layer convergence then shifts the convection northward, driving the northward propagation of the BSISO. This vorticity-convection interaction has played a central role in our understanding of the BSISO thus far. Figure 9a shows, on the other hand, that TRMM precipitation is largely in phase with barotropic vorticity—computed here as vorticity averaged between 800 and 200 hPa—in ERAI. This in-phase relation between vorticity and precipitation is also present in bandpass-filtered fields (Figure 9c): Barotropic vorticity and rain are largely in phase north of 5°N with a marginal lead by 2–3 days, while vorticity lead rain within 5°S–5°N. The simulated barotropic vorticity and rain from the ensemble mean are noisier (Figure 9b), but the

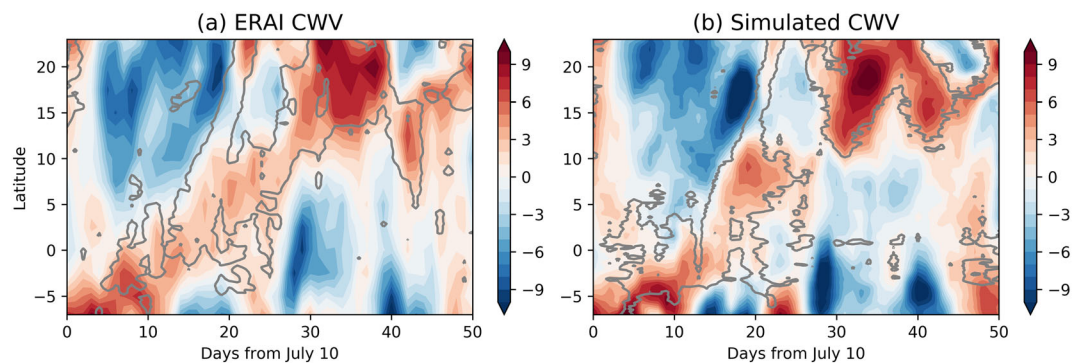


Figure 10. Anomalies of column-integrated water vapor (CWV) and rain (contour, 10 mm/day) averaged between 110°E and 130°E from the (a) ERA-I and (b) coupled ensemble. The anomalies are computed by subtracting the mean during 10 July and 31 August.

There is strong latitude dependence in the magnitude of the positive moisture anomalies; they exceed 6 mm south of the equator, weaken to less than 2 mm after passing the equator, and then strengthen again to reach their maximum amplitude (9 mm) near 20°N. Inspection of 20–90 day bandpass-filtered moisture anomalies with ERAI indicates that this latitudinal dependence is a common feature of northward propagating BSISO events (not shown).

We analyze the budget of column-integrated moisture in these simulations, which may be written as

$$\begin{aligned} \left\langle \frac{\partial q_v}{\partial t} \right\rangle &= -HADV_q - VADV_q + E - P \\ VADV_q &= - \left\langle \vec{v}_h \nabla q_v \right\rangle, \text{ and } HADV_q = - \left\langle \omega \frac{\partial q_v}{\partial p} \right\rangle, \end{aligned} \quad (1)$$

where $\langle \rangle$ denotes mass weighted vertical integral from surface to 100 hPa; $HADV_q$ and $VADV_q$ are horizontal and vertical advection at the horizontal scales resolved by the model; E is surface evaporation by the subgrid-scale eddies; P is precipitation. We have neglected the diffusion process in the horizontal or vertical directions, assuming that it is not important in a large domain. Vertical integrals from the surface to 850 hPa are also computed to assess the PBL contribution to horizontal advection—those are general very small and will not be discussed further. Daily mean values of E and P can be accurately calculated from the accumulation of the 3-hourly values. However, estimating the advection terms from the 3-hourly output of the coupled simulations is not straightforward, primarily because advection is numerically expressed in flux form in the WRF dynamical core (as in most modern numerical modeling systems), which precludes direct online estimates of the advection terms. Instead, we estimate these budget terms in a box using 3-hourly data at the WRF dry-mass levels. The moisture budget is estimated in large boxes covering different latitudes: 0–10°N, 10–15°N, 15–20°N, and all averaged over the longitude range 110–120°E.

The largest term in absolute magnitude on the r.h.s. of (1) in the precipitating area is the precipitation itself, which is a moisture sink and always negative definite. The second largest term is vertical advection. These two terms cancel out to a great degree, as moisture brought up by vertical advection is removed by precipitation. The residual of these two terms is typically 1 order of magnitude smaller than the individual terms and remains negative in our simulations. We group the four r.h.s terms into two categories: the column processes, including vertical advection, E and P , and horizontal advection. The column processes are local—they only involve physics in the columns. In models of the tropical atmosphere, it is often tacitly assumed that the primary balance of moisture is within the column (e.g., Neelin & Zeng, 2000, among many others). Building this assumption into theoretical models is adequate for explaining a variety of synoptic convectively coupled wave phenomena. Horizontal advection, on the other hand, can also be important, as shown in some modeling studies (e.g., Pritchard & Bretherton, 2014; S. Wang et al., 2013; S. Wang et al., 2016) and observational analyses of the MJO (e.g., Back & Bretherton, 2006; Sobel et al., 2014). An analysis of the moisture budget also indicates that horizontal advection is significantly correlated with low frequency modes of variability such as the MJO (Yasunaga et al., 2019) in the coherence spectrum. The recent studies by Adames et al. (2016) and Jiang et al. (2018) have suggested importance of horizontal moisture advection

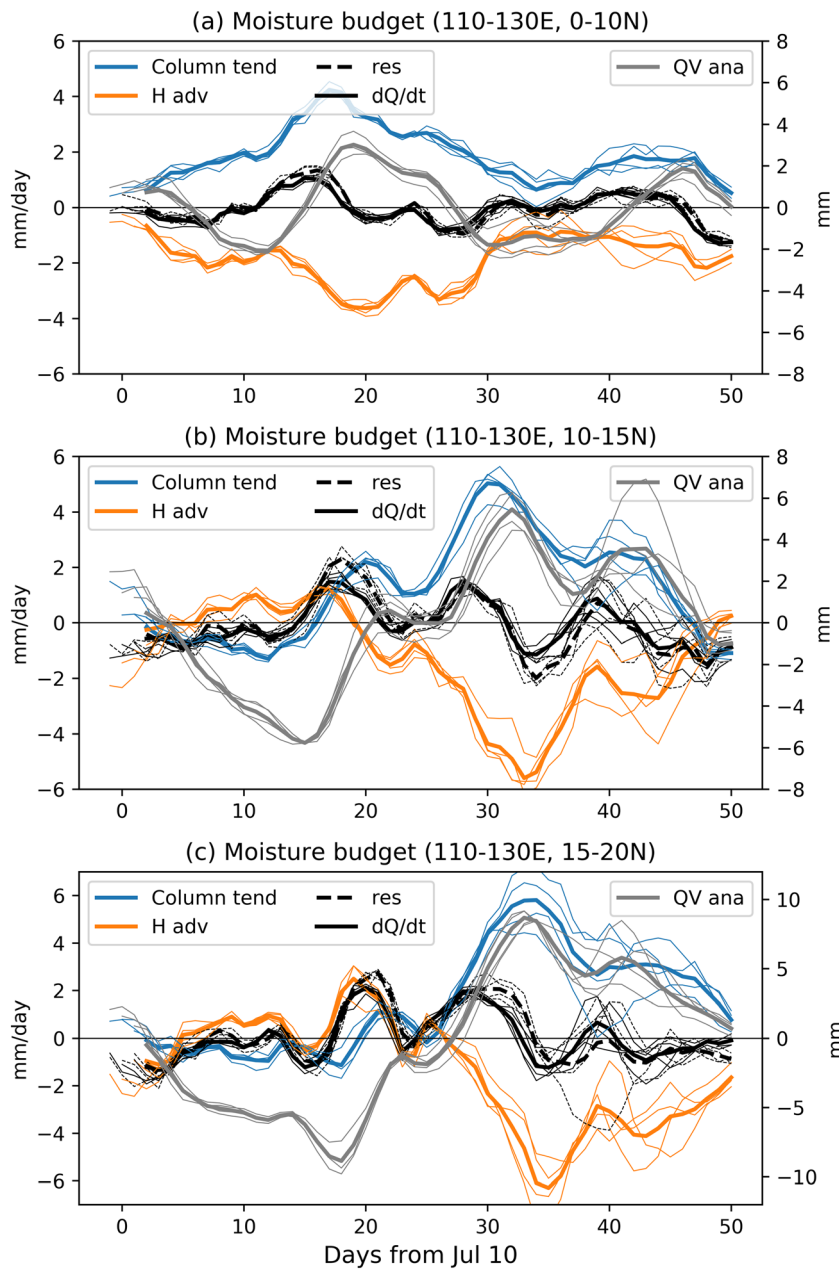


Figure 11. Time series of column-integrated moisture budget terms from the WRF simulations, including column processes, horizontal transport, residual of r.h.s in Equation 1 and tendency derived from moisture, in three latitude regions, (a) 0–10°N, (b) 10–15°N, and (c) 15–20°N. Anomaly of column moisture is shown in gray. All the time series are smoothed with a 5-day running average.

for the northward propagation of the BSISO, although they mainly focused over the Indian Ocean. We will show below that horizontal advection is important to this BSISO as well.

Figure 11a shows that anomalies of column moisture, computed by subtracting the time mean during the integration, exhibit several cycles on the intraseasonal time scale. We focus on the northward propagating moisture anomaly identified in Figure 10. Near the equator (0–10°N), the moisture anomaly has a small amplitude (2–3 mm) and reaches its minimum at Day 12 into the simulation, after which it gradually increases due to moistening primarily by column processes, reaching its peak at approximately Day 18. Afterward, the column processes continue to make a positive contribution until Day 33, while horizontal

advection of dry air contributes to the reduction of the moisture anomaly after this time. These two relatively large terms cancel to a large extent, leaving a relatively small positive tendency between Days 33 and 45. The residual of the column and horizontal transport (black dashed) compares well with the tendency derived directly from the time series of column-integrated moisture (dQ/dt , bold black), indicating that our estimates of these advection processes are reasonably accurate.

The BSISO moisture anomaly averaged between 10°N and 15°N reaches its peak value (~7 mm) around Day 33 (Figure 11b). Horizontal advection is positive during the dry phase and then during the first half of the period in which moisture increases, becoming negative after Day 20. Column processes reduce moisture before Day 17 and then become positive, and the primary contributor to the increase of moisture, from Day 17, covarying with moisture anomalies after that point. This comparison indicates that horizontal advection plays an important role in the change of sign of the moisture anomaly from the dry to the moist phase and, thus, in the northward propagation of the active phase. The moisture anomaly farther north ($15\text{--}20^{\circ}\text{N}$, $110\text{--}120^{\circ}\text{E}$) is overall similar except that it is delayed by a few days, and corresponding budget terms show a delay as well.

Time series of the moisture anomalies and the tendencies (column processes and horizontal advection) in these different latitudes suggests that during the active phase, column processes first contribute to the positive tendency of moisture, followed by the horizontal drying in the post-active phase. During the suppressed phase (before Day 20 in Figure 11b and before Day 25 in Figure 11c), the roles of column processes and HADV are opposite: The former contributes to drying and the latter to moistening. This phase relationship between HADV and moisture anomalies suggests that HADV helps the northward propagation of moisture anomalies.

5.3. Lead/Lag Analysis of Vorticity and Horizontal Advection in the Longer Record

It is possible that the above results are case dependent. To see to what extent this may be so, we further analyze the lead/lag correlation between TRMM precipitation and ERAI vorticity/moisture on the intraseasonal timescale using all boreal summer data (July–August) from 1998 to 2017. All fields are bandpass filtered using a nonrecursive 20- to 90-day Lanczos filter. We consider the lead/lag relation in two regions: over the Maritime Continent region ($110\text{--}130^{\circ}\text{E}$) and over the Indian Ocean ($70\text{--}90^{\circ}\text{E}$). The lead-lag correlations (Figure 12) are derived at each latitude independently against their corresponding rainfall anomalies at the same latitude in these two regions. Precipitation from the ERA-I reanalysis is not used because of its greater biases compared to TRMM. As a result, our estimates of column moisture processes that include precipitation are not accurate. We focus on the horizontal advection and its relationship with precipitation.

Figure 12a shows that the positive correlation between precipitation and barotropic vorticity averaged between 110°E and 130°E achieves its maximum at Day 0 north of 5°N and becomes negative 20 days before and after maximum precipitation. This in-phase relation between precipitation and vorticity is consistent with the results of the case study above. On the other hand, the precipitation correlation in the eastern Indian Ocean ($70\text{--}90^{\circ}\text{E}$) is somewhat different: positive vorticity leads precipitation by a few days between 5°N and 10°N , while they are in phase north of 15°N . This lead in vorticity relative to precipitation in the eastern Indian Ocean is consistent with the results of Jiang et al. (2004) and was also noticed by DeMott et al. (2013), who showed that in a composite analysis at a reference latitude of 5°N over the Indian Ocean, barotropic vorticity leads the BSISO convection. In both longitude bands, however, the barotropic vorticity leads convection when the maximum precipitation anomaly is at lower latitudes while the two become more in phase as the anomaly moves northward. Interestingly, this qualitative behavior is present in the idealized axisymmetric, atmosphere-only model of Bellon and Sobel (2008b), if one examines the relationship between upper-level divergence and lower-level vorticity (their Figures 5–9). Those authors briefly noted this feature but did not explain it; the fact that it is present in their model suggests that it can be explained in terms of the processes in their model—including a version of the convective physics from the quasi-equilibrium tropical circulation model (Neelin & Zeng, 2000; Zeng et al., 2000)—though such an explanation awaits future work.

Figures 12c and 12d show that in both longitude bands, positive horizontal advection of moisture leads precipitation by 10–20 days, while negative advection lags maximum precipitation by 5–10 days. This phase lead of horizontal advection relative to rain is also consistent with the case simulated in the earlier part of this

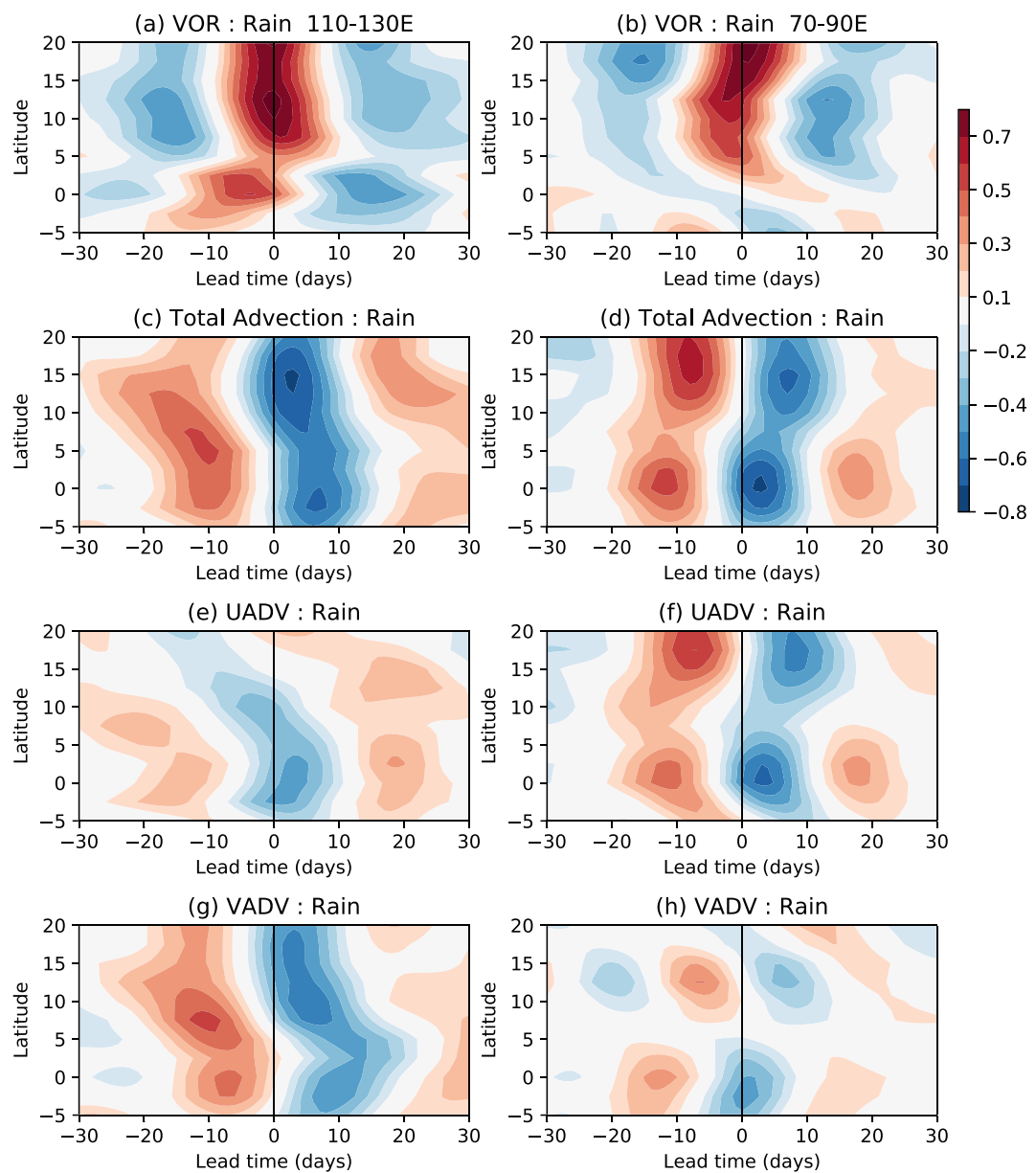


Figure 12. Correlation between rain and four variables (vorticity, moisture budget terms) derived from ERAI. (left panels) Lag correlation between 20–90 day bandpass-filtered precipitation and (a) barotropic vorticity, (b) column-integrated horizontal advection of moisture, (c) zonal component of horizontal moisture advection, and (d) meridional component of horizontal moisture advection averaged over 110–130°E in the Maritime Continent region. (right panels) As left but for the region 70–90°E in the Indian Ocean region. Negative leads denote that the other variable in question leads precipitation.

study, particularly north of 10°N. Regional dependence in the lead/lag correlation is evident. The maximum correlation between horizontal advection and rain occurs at lead day 10 and latitude 5 N in the MC region, and the time lead increases farther north; while the maximum lead is at Day 10 in the Indian Ocean. The horizontal advection may be further broken into two terms: zonal advection (UADV) and meridional advection (VADV). Figures 12e and 12f show that UADV is strong in the Indian Ocean, while the correlation between VADV and rain is weak at all leads/lags in this region. On the contrary, VADV dominates in the MC region, while the correlation between UADV and rain is less than 0.3 north of 10°N. This regional dependence in the relationship between horizontal advection and rain is presumably related

to the climatological distribution of moisture: There is a stronger zonal gradient in the Indian Ocean but a greater meridional gradient in the MC region. The phase lead of HADV is generally consistent with the case study shown above.

6. Conclusions

During the summer of 2016, a BSISO event was observed over the Maritime Continent region. Precipitation anomalies associated with this BSISO event propagated northward at a speed of approximately 1°/day from July to August. To understand the dynamical processes associated with this BSISO event, coupled numerical simulations of one full BSISO life cycle were conducted to explore atmospheric processes and air-sea interaction. The coupled modeling system consists of the Weather Research and Forecasting (WRF) model and the HYCOM. The results may be summarized as follows:

1. The 50-day long 4-member coupled simulations reasonably capture the large-scale northward propagation of this BSISO event in precipitation, low-level winds, and MLD in the ocean over the South China Sea region.
2. Coupled simulations with altered air-sea interaction and uncoupled simulations with prescribed sea surface temperature were further conducted to examine mechanisms. Experiments without topography in the MC region simulate slightly faster northward propagation. Completely removing islands in the MC region in the uncoupled simulations leads to stronger wind anomalies at lower levels and slightly faster northward propagation. Nonetheless, none of these sensitivity experiments substantially change the fundamental character of the northward propagation. The changes in the BSISO in the experiment in which intraseasonal SST anomalies are completely eliminated are less dramatic compared to those experiments removing topography or land. This suggests that ocean coupling is less important to the northward propagation of this BSISO event in the MC region than are land processes. S. Wang et al. (2015) showed that daily SST variations play distinct roles in two MJO events, however, so it is possible that the importance of the SST feedback to the BSISO is similarly case-dependent.
3. Diagnostics of precipitation and vorticity from the simulations and ERAI reanalysis indicate that the two variables are mostly in phase during the BSISO convective phase, especially at latitudes north of 10°N. This differs from the conventional view that barotropic vorticity ought to lead convection for northward propagation.
4. Substantial moisture anomalies are associated with the BSISO rain anomalies. Northward propagating moisture anomalies are in phase with precipitation during this BSISO event. The amplitudes of moisture anomalies range from 3–4 mm near the equator to nearly 10 mm at ~15°N. Moisture budget terms (other than the tendency) are grouped into two terms: local column processes and horizontal advection. It is shown that the two terms are of the same order of magnitude. Horizontal advection is positive during the suppressed phase, while local column processes are responsible for the sharp increases in moisture anomalies during the transition period from the suppressed to the active phase.
5. Analysis of 20-year TRMM precipitation and ERAI data is used to test to what extent the above findings may be generalized. The lead/lag correlation structure between rain and barotropic vorticity shows that the two are generally in phase in the MC region over this period of time. Significant regional differences in lead/lag correlation are found, however. Both the coupled simulations and these observational data lend further support to the notion that horizontal moisture advection plays a significant role in BSISO propagation, especially at latitudes north of 10°N, while the shear-vorticity-convection interaction mechanism described in a number of earlier studies appears to be unimportant at those latitudes.

Data Availability Statement

Simulation data sets from these simulations are available at <http://doi.org/10.5281/zenodo.3891748>; TRMM 3B42 precipitation data (<https://pps.gsfc.nasa.gov/>); the ERA-Interim is available at ECMWF (<https://www.ecmwf.int/en/forecasts/datasets/reanalysis-datasets/era-interim>); the OMI index (Kiladis et al., 2014) (<https://www.esrl.noaa.gov/psd/mjo/mjoindex/>); the BSISO1 index (Lee et al., 2013) (<http://www.apcc21.org/ser/moni.do?lang=en>); and the BSISO index (Kikuchi et al., 2012) (http://iprc.soest.hawaii.edu/users/kazuyosh/Bimodal_ISO.html).

Acknowledgments

S. W. and A. H. S. acknowledge support from ONR N00014-16-1-3073 and NSF AGS-1543932. We acknowledge high-performance computing support from Cheyenne (ark:/85065/d7wd3xhc) provided by NCAR's Computational and Information Systems Laboratory, sponsored by the National Science Foundation. We thank three anonymous reviewers for their insightful comments and suggestions.

References

- Adames, Á. F., Wallace, J. M., & Monteiro, J. M. (2016). Seasonality of the structure and propagation characteristics of the MJO. *Journal of the Atmospheric Sciences*, 73, 3511–3526.
- Back, L. E., & Bretherton, C. S. (2006). Geographic variability in the export of moist static energy and vertical motion profiles in the tropical Pacific. *Geophysical Research Letters*, 33, L17810. <https://doi.org/10.1029/2006GL026672>
- Bellon, G., & Sobel, A. H. (2008a). Instability of the axisymmetric monsoon flow and intraseasonal oscillation. *Journal of Geophysical Research*, 113, D07108. <https://doi.org/10.1029/2007JD009291>
- Bellon, G., & Sobel, A. (2008b). Poleward-propagating intraseasonal monsoon disturbances in an intermediate-complexity axisymmetric model. *Journal of the Atmospheric Sciences*, 65, 470–489. <https://doi.org/10.1175/2007JAS2339.1>
- Bellon, G., Sobel, A. H., & Vialard, J. (2008). Ocean-atmosphere coupling in the monsoon intraseasonal oscillation: A simple model study. *Journal of Climate*, 21, 5254–5270. <https://doi.org/10.1175/2008JCLI2305.1>
- Bellon, G., & Srinivasan, J. (2006). Comments on “Structures and mechanisms of the northward propagating boreal summer intraseasonal oscillation”. *Journal of Climate*, 19, 4738–4743. <https://doi.org/10.1175/JCLI3861.1>
- Boos, W. R., & Kuang, Z. (2010). Mechanisms of poleward propagating, intraseasonal convective anomalies in cloud system-resolving models. *Journal of the Atmospheric Sciences*, 67, 3673–3691.
- Chen, F., & Dudhia, J. (2001). Coupling an advanced land surface-hydrology model with the Penn State-NCAR MM5 modeling system. Part I. Model implementation and sensitivity. *Monthly Weather Review*, 129(4), 569–585. [https://doi.org/10.1175/1520-0493\(2001\)129<0569:caalsh>2.0.co;2](https://doi.org/10.1175/1520-0493(2001)129<0569:caalsh>2.0.co;2)
- Chen, S. S., & Curgic, M. (2016). Ocean surface waves in Hurricane Ike (2008) and Superstorm Sandy (2012): Coupled modeling and observations. *Ocean Model*, 103, 161–176. <https://doi.org/10.1016/j.ocemod.2015.08.005>
- Chen, X., Pauluis, O. M., & Zhang, F. (2018a). Atmospheric overturning across multiple scales of an MJO event during the CINDY/DYNAMO campaign. *Journal of the Atmospheric Sciences*, 75, 381–399. <https://doi.org/10.1175/JAS-D-17-0060.1>
- Chen, X., Pauluis, O. M., & Zhang, F. (2018b). Regional simulation of Indian summer monsoon intraseasonal oscillations at gray-zone resolution. *Atmospheric Chemistry and Physics*, 18(2), 1003–1022. <https://doi.org/10.5194/acp-18-1003-2018>
- Chen, X., Zhang, F., & Ruppert, J. H. (2019). Modulations of the diurnal cycle of coastal rainfall over South China caused by the boreal summer Intraseasonal oscillation. *Journal of Climate*, 32, 2089–2108. <https://doi.org/10.1175/JCLI-D-18-0786.1>
- Curgic, M., Chen, S. S., & Özgökmen, T. M. (2016). Hurricane-induced ocean waves and stokes drift and their impacts on surface transport and dispersion in the Gulf of Mexico. *Geophysical Research Letters*, 43, 2773–2781. <https://doi.org/10.1002/2015GL067619>
- Dee, D. P., Uppala, S. M., Simmons, A. J., Berrisford, P., Poli, P., Kobayashi, S., et al. (2011). The ERA-Interim reanalysis: configuration and performance of the data assimilation system. *Quarterly Journal of the Royal Meteorological Society*, 137(656), 553–597. <https://doi.org/10.1002/qj.828>
- DeMott, C. A., Stan, C., & Randall, D. A. (2013). Northward propagation mechanisms of the boreal summer intraseasonal oscillation in the ERA-Interim and SP-CCSM. *Journal of Climate*, 26, 1973–1992. <https://doi.org/10.1175/JCLI-D-12-00191.1>
- Donlon, C. J., Martin, M., Stark, J., Roberts-Jones, J., Fiedler, E., & Wimmer, W. (2012). The operational sea surface temperature and sea ice analysis (OSTIA) system. *Remote Sensing of Environment*, 116, 140–158. <https://doi.org/10.1016/j.rse.2010.10.017>
- Fu, X., & Wang, B. (2004). The boreal-summer intraseasonal oscillations simulated in a hybrid coupled atmosphere-ocean model. *Monthly Weather Review*, 132, 2628–2649.
- Fu, X., Wang, B., & McCreary, J. P. (2003). Coupling between northward-propagating, intraseasonal oscillations and sea surface temperature in the Indian Ocean. *Journal of the Atmospheric Sciences*, 60, 1733–1753.
- Fu, X., Wang, B., Waliser, D. E., & Tao, L. (2007). Impact of atmosphere-ocean coupling on the predictability of monsoon intraseasonal oscillations. *Journal of the Atmospheric Sciences*, 64, 157–174.
- Hsu, P., Lee, J., & Ha, K. (2016). Influence of boreal summer intraseasonal oscillation on rainfall extremes in southern China. *International Journal of Climatology*, 36, 1403–1412. <https://doi.org/10.1002/joc.4433>
- Huffman, G. J., Adler, R. F., Bolvin, D. T., Gu, G. J., Nelkin, E. J., Bowman, K. P., et al. (2007). The TRMM multisatellite precipitation analysis (TMPA): Quasi-global, multiyear, combined-sensor precipitation estimates at fine scales. *Journal of Hydrometeorology*, 8, 38–55.
- Iacono, M. J., Delamere, J. S., Mlawer, E. J., Shephard, M. W., Clough, S. A., & Collins, W. D. (2008). Radiative forcing by long-lived greenhouse gases: Calculations with the AER radiative transfer models. *Journal of Geophysical Research*, 113, D13103. <https://doi.org/10.1029/2008JD009944>
- Jiang, X., Adames, A. F., Zhao, M., Waliser, D., & Maloney, E. (2018). A unified moisture mode framework for seasonality of MJO propagation. *Journal of Climate*, 31. <https://doi.org/10.1175/JCLI-D-17-0671.1>
- Jiang, X., Li, T., & Wang, B. (2004). Structures and mechanisms of the northward propagating boreal summer intraseasonal oscillation. *Journal of Climate*, 17, 1022–1039.
- Kang, I.-S., Kim, D., & Kug, J.-S. (2010). Mechanism for northward propagation of boreal summer intraseasonal oscillation: Convective momentum transport. *Geophysical Research Letters*, 37, L24804. <https://doi.org/10.1029/2010GL045072>
- Kemball-Cook, S., & Wang, B. (2001). Equatorial waves and air-sea interaction in the boreal summer intraseasonal oscillation. *Journal of Climate*, 14, 2923–2942.
- Kikuchi, K., Wang, B., & Kajikawa, Y. (2012). Bimodal representation of the tropical intraseasonal oscillation. *Climate Dynamics*, 38, 1989–2000. <https://doi.org/10.1007/s00382-011-1159-1>
- Kiladis, G. N., Dias, J., Straub, K. H., Wheeler, M. C., Tulich, S. N., Kikuchi, K., et al. (2014). A comparison of OLR and circulation-based indices for tracking the MJO. *Monthly Weather Review*, 142, 1697–1715. <https://doi.org/10.1175/MWR-D-13-00301.1>
- Krishnamurti, T. N., & Subramanian, D. (1982). The 30–50 day mode at 850 mb during MONEX. *Journal of the Atmospheric Sciences*, 39, 2088–2095.
- Lau, K.-M., & Chan, P. H. (1986). Aspects of the 40–50 day oscillation during the northern summer as inferred from outgoing longwave radiation. *Monthly Weather Review*, 114, 1354–1367.
- Lee, J. Y., Wang, B., Wheeler, M. C., Fu, X., Waliser, D. E., & Kang, I.-S. (2013). Real-time multivariate indices for the boreal summer intraseasonal oscillation over the Asian summer monsoon region. *Climate Dynamics*, 40, 493–509. <https://doi.org/10.1007/s00382-012-1544-4>
- Li, C., Li, T., Lin, A., Gu, D., & Zheng, B. (2015). Relationship between summer rainfall anomalies and sub-seasonal oscillations in South China. *Climate Dynamics*, 44(1–2), 423–439. <https://doi.org/10.1007/s00382-014-2172-y>

- Li, G., Curcic, M., Iskandarani, M., Chen, S. S., & Knio, O. M. (2019). Uncertainty propagation in coupled atmosphere–wave–ocean prediction system: A study of Hurricane Earl (2010). *Monthly Weather Review*, 147, 221–245. <https://doi.org.ezproxy.cul.columbia.edu/10.1175/MWR-D-17-0371.1>
- Li, Y., Han, W., Ravichandran, M., Wang, W., Shinoda, T., & Lee, T. (2017). Bay of Bengal salinity stratification and Indian summer monsoon intraseasonal oscillation: 1. Intraseasonal variability and causes. *Journal of Geophysical Research: Oceans*, 122, 4291–4311. <https://doi.org/10.1002/2017JC012691>
- Liebmann, B., & Smith, C. A. (1996). Description of a complete (interpolated) outgoing long-wave radiation dataset. *Bulletin of American Meteorological Society*, 77, 1275–1277.
- Lim, K.-S. S., & Hong, S.-Y. (2010). Development of an effective double-moment cloud microphysics scheme with Prognostic Cloud Condensation Nuclei (CCN) for weather and climate models. *Monthly Weather Review*, 138(5), 1587–1612. <https://doi.org/10.1175/2009mwr2968.1>
- Miura, H., Satoh, M., Nasuno, T., Noda, A. T., & Oouchi, K. (2007). A Madden–Julian Oscillation event realistically simulated by a global cloud-resolving model. *Science*, 318(5857), 1763–1765. <https://doi.org/10.1126/science.1148443>
- Nakano, M., Sawada, M., Nasuno, T., & Satoh, M. (2015). Intraseasonal variability and tropical cyclogenesis in the western North Pacific simulated by a global nonhydrostatic atmospheric model. *Geophysical Research Letters*, 42, 565–571. <https://doi.org/10.1002/2014GL062479>
- Neelin, J. D., & Zeng, N. (2000). A quasi-equilibrium tropical circulation model—Formulation. *Journal of the Atmospheric Sciences*, 57, 1741–1766.
- Pleim, J. E. (2007). A combined local and nonlocal closure model for the atmospheric boundary layer. Part I: Model description and testing. *Journal of Applied Meteorology and Climatology*, 46, 1383–1395. <https://doi.org/10.1175/JAM2539.1>
- Pritchard, M. S., & Bretherton, C. S. (2014). Causal evidence that rotational moisture advection is critical to the Superparameterized Madden–Julian Oscillation. *Journal of the Atmospheric Sciences*, 71(2), 800–815. <https://doi.org/10.1175/jas-d-13-0119.1>
- Pullen, J., Gordon, A. L., Flatau, M., Doyle, J. D., Villanoy, C., & Cabrera, O. (2015). Multiscale influences on extreme winter rainfall in the Philippines. *Journal of Geophysical Research: Atmospheres*, 120, 3292–3309. <https://doi.org/10.1002/2014JD022645>
- Skamarock, W. C., Klemp, J. B., Dudhia, J., Gill, D. O., Barker, D. M., Wang, W., & Powers, J. G. (2008). A description of the advanced research WRF version 3. NCAR Tech. Note NCAR/TN-475STR, 125 p.
- Sobel, A., Wang, S., & Kim, D. (2014). Moist static energy budget of the MJO during DYNAMO. *Journal of the Atmospheric Sciences*, 71(11), 4276–4291. <https://doi.org/10.1175/jas-d-14-0052.1>
- Sobel, A. H., Burleyson, C. D., & Yuter, S. E. (2011). Rain on small tropical islands. *Journal of Geophysical Research*, 116, D08102. <https://doi.org/10.1029/2010JD014695>
- Sobel, A. H., Maloney, E., Bellon, G., & Frierson, D. F. M. (2010). Surface fluxes and tropical intraseasonal variability: A reassessment. *Journal of Advances in Modeling Earth Systems*, 2, 2. <https://doi.org/10.3894/JAMES.2010.2.2>
- Wallcraft, A. J., Metzger, E. J., & Carroll, S. N. (2009). Software design description for the HYbrid Coordinate Ocean Model (HYCOM) version 2.2, Tech. Rep., NRL/MR/732009–9166.
- Wang, B., & Rui, H. (1990). Synoptic climatology of transient tropical intraseasonal convection anomalies: 1975–1985. *Meteorology and Atmospheric Physics*, 44(1–4), 43–61. <https://doi.org/10.1007/bf01026810>
- Wang, B., & Xie, X. (1997). A model for the boreal summer intraseasonal oscillation. *Journal of the Atmospheric Sciences*, 54, 72–86.
- Wang, S., Ma, D., Sobel, A. H., & Tippett, M. K. (2018). Propagation characteristics of BSISO indices. *Geophysical Research Letters*, 45, 9934–9943. <https://doi.org/10.1029/2018GL078321>
- Wang, S., & Sobel, A. H. (2017). Factors controlling rain on small tropical islands: Diurnal cycle, large-scale wind speed, and topography. *Journal of the Atmospheric Sciences*. <https://doi.org/10.1175/JAS-D-16-0344.1>
- Wang, S., Sobel, A. H., & Kuang, Z. (2013). Cloud-resolving simulation of TOGA-COARE using parameterized large-scale dynamics. *Journal of Geophysical Research: Atmospheres*, 118, 6290–6301. <https://doi.org/10.1002/jgrd.50510>
- Wang, S., Sobel, A. H., & Nie, J. (2016). Modeling the MJO in a cloud-resolving model with parameterized large-scale dynamics: Vertical structure, radiation, and horizontal advection of dry air. *Journal of Advances in Modeling Earth Systems*, 8, 121–139. <https://doi.org/10.1002/2015ms000529>
- Wang, S., Sobel, A. H., Tippett, M. K., & Vitart, F. (2019). Prediction and predictability of tropical intraseasonal convection: Seasonal dependence and the Maritime Continent prediction barrier. *Climate Dynamics*, 52, 6015. <https://doi.org/10.1007/s00382-018-4492-9>
- Wang, S., Sobel, A. H., Zhang, F., Sun, Y. Q., Yue, Y., & Zhou, L. (2015). Regional simulation of the October and November MJO events observed during the CINDY/DYNAMO field campaign at gray zone resolution. *Journal of Climate*, 28, 2097–2119.
- Wang, T., Yang, X., Fang, J., Sun, X., & Ren, X. (2018). Role of air–sea interaction in the 30–60-day boreal summer intraseasonal oscillation over the Western North Pacific. *Journal of Climate*, 31, 1653–1680. <https://doi.org/10.1175/JCLI-D-17-0109.1>
- Webster, P. J. (1983). Mechanisms of monsoon transition: Surface hydrology effects. *Journal of the Atmospheric Sciences*, 40, 2110–2124.
- Yasunaga, K., Yokoi, S., Inoue, K., & Mapes, B. E. (2019). Space–time spectral analysis of the moist static energy budget equation. *Journal of Climate*, 32, 501–529. <https://doi.org/10.1175/JCLI-D-18-0334.1>
- Yasunari, T. (1979). Cloudiness fluctuations associated with the northern hemisphere summer monsoon. *Journal of the Meteorological Society of Japan*, 57, 227–242.
- Zeng, N., Neelin, J. D., & Chou, C. (2000). A quasi-equilibrium tropical circulation model—Implementation and simulation. *Journal of the Atmospheric Sciences*, 57, 1767–1796.
- Zhang, F., Taraphdar, S., & Wang, S. (2017). The role of global circumnavigating mode in the MJO initiation and propagation. *Journal of Geophysical Research: Atmospheres*, 122, 5837–5856. <https://doi.org/10.1002/2016JD025665>
- Zhang, L., Han, W., Li, Y., & Maloney, E. D. (2018). Role of north Indian Ocean air-sea interaction in summer monsoon intraseasonal oscillation. *Journal of Climate*, 31, 7885–7908.